Materials Science

http://www.aimspress.com/journal/Materials

AIMS Materials Science, 10(1): 1–25.
DOI: 10.3934/matersci.2023001
Received: 03 August 2022
Revised: 19 September 2022
Accepted: 06 October 2022
Published: 11 November 2022

Research article

Influence of the thermomechanical behavior of NiTi wires embedded in a damper on its damping capacity: Application to a bridge cable

Guillaume Helbert[1,*], Lamine Dieng[2], Shabnam Arbab Chirani[1] and Philippe Pilvin[3]

[1] ENI Brest, UMR CNRS 6027, IRDL, Technopôle Brest-Iroise, 29238 Brest, France

[2] Université Gustave Eiffel, MAST, Allée des Ponts et Chaussées, 44340 Bouguenais, France

[3] Université Bretagne Sud, UMR CNRS 6027, IRDL, Centre de Recherche Christian Huygens, Rue de Saint-Maudé, 56100 Lorient, France

* **Correspondence:** Email: guillaume.helbert@enib.fr; Tel: +33-2-98-05-66-55.

Abstract: Thanks to high dissipation properties, embedding NiTi Shape Memory Alloys in passive damping devices is effective to mitigate vibrations in building and cable structures. These devices can inconceivably be tested directly on full-scale experimental structures or on structures in service. To predict their effectiveness and optimize the set-up parameters, numerical tools are more and more developed. Most of them consist of Finite Element models representing the structure equipped with the damping device, embedding parts associated with a superelastic behavior. Generally, the implemented behavior laws do not include all the phenomena at the origin of strain energy dissipation, but stress-induced martensitic transformation only. This article presents a thermomechanical behavior law including the following phenomena: (i) intermediate R-phase transformation, (ii) thermal effects and (iii) strain localization. This law was implemented in a commercial Finite Element code to study the dynamic response of a bridge cable equipped with a NiTi wire-based damping device. The numerical results were compared to full-scale experimental ones, by considering the above-mentioned phenomena taken coupled or isolated: it has been shown that it is necessary to take all of these phenomena into account in order to successfully predict the damping capacity of the device.

Keywords: bridge cable; damping device; shape memory alloys; dissipation; finite element; full-scale tests

1. Introduction

The damping capacity of a material is its ability to absorb mechanical energy by dissipation of elastic strain energy [1]. In Shape Memory Alloys (SMA), the dissipated energy is associated with their

hysteretic superelastic behavior [2]. Superelasticity is the remarkable property of the material to experience a large and quasi reversible strain (6–10% or much more in the case of single crystals SMAs [3]) under isothermal mechanical loadings, above a characteristic temperature of the alloy called "Austenite finish" (A_f) [4, 5]. This phenomenon is due to a reversible transformation from the parent-phase "Austenite" to a more disordered phase called "Martensite", and more particularly to the re-orientation of the obtained lattices above a critical stress value (transformation yield stress). Thus, SMAs are good candidates to damp oscillations experienced by buildings and Civil Engineering structures [6]. In particular, NiTi-based SMAs are very attractive due to their remarkable dissipative properties, re-centering ability and they combine relatively good resistance to fatigue, corrosion and fire. However, NiTi alloys are known to be very temperature-sensitive: the slope that characterizes the increase in transformation yield stress with temperature is about 7–8 MPa $\cdot$ K^{-1} [7]. Over the years, SMA-based vibration control devices (passive, active or hybrid) have been designed to protect Civil Engineering structures from different types of external solicitations [8].

Cables are crucial parts of bridge structures (such as stay cable bridges, suspension bridges, and prestressed concrete bridges) but they experience vibrations entailed by traffic or a combination of wind and rain [9]. To increase the structural damping ratio of the cables, SMA-based external passive damping devices are well suited: they exert a transverse damping force on the cable near its anchorages to fight against transverse displacements and therefore improve its fatigue resistance. To predict the effectiveness and to optimize the use of SMA-based damping devices, numerical tools are generally required to solve strongly non-linear problems. As stated in [10, 11], it is necessary to consider the most accurate mechanical behavior (through its stiffness and loss factor changes) of the embedded SMA components to correctly capture the dynamic response of the whole system. Since it is not appropriate to identify the various model parameters describing the hysteresis loops for each of the possible test conditions, the material law should take into account all the phenomena that can affect its properties and only involve parameters intrinsic to the material. Among these phenomena, one can cite:

(1) Thermal effects:
As stated previously, the superelasticity phenomenon in NiTi-based SMAs is temperature-sensitive: martensite transformation yield stress is a linear function of the material temperature [12]. Since the forward and reverse martensitic transformations are exothermic and endothermic processes respectively [13], the temperature of the material changes under mechanical loadings according to the heat exchange with its surroundings. The martensitic transformation yield stress changes as a consequence, which leads naturally to thermomechanical couplings. Thus, the slope associated to the martensitic transformation plateau and the amplitude of temperature variations over a loading cycle increase with strain rate [12]. Furthermore, the hysteresis behavior in SMA is accompanied by intrinsic dissipation [14] that entails "self-heating" of the material under cyclic mechanical loadings. It naturally shifts up the hysteresis loops and slightly affects their shape. Combination of these two phenomena is responsible for a non-monotonous change of energy dissipated by the material versus strain rate [15]. Numerous models have considered these effects [16–19].

(2) R-phase transformation:
NiTi alloys can experience an additional phase transformation allowing the formation of R-phase with a trigonal crystallographic structure [20, 21]. R-phase is often qualified as an "intermediate phase" because the yield stress associated with its transformation from austenite is lower than the martensitic transformation yield stress at room temperature [15]. The range of recoverable strain due to R-phase transformation is 0–1.5%, according to [22]. The presence of R-phase can affect the stiffness of the material: the corresponding elasticity modulus is estimated to be between 20 and 40 GPa. R-phase is associated with a low intrinsic dissipation because of a narrow hysteresis loop area but the corresponding damping capacity is not negligible. R-phase transformation is more sensitive to temperature than martensitic transformation: the slope related to R-phase domains on phases pseudo-diagram is reported to be in the range 13–17 $MPa{\cdot}K^{-1}$ [15, 22]. Some numerical models have considered R-phase and most of them are phenomenological ones [23–26].

(3) Strain localization:
It is commonly agreed that martensitic transformation occurs with nucleation of martensite, followed by propagation of a martensitic front [27]. After [29], high shear stress values at the interface between austenite and stress-induced martensite are responsible for this localized process in NiTi wires. Under tensile loadings, the ratio of the maximum equivalent stress to the axial equivalent stress was estimated to be approximatively 1.4 to 1.6 in wires. In addition to a heterogeneous strain field, a heterogeneous thermal field was reported in [28]. Thus, these thermal effects can affect the propagation of the martensitic front, since martensite is more stable at low temperatures while the forward martensitic transformation is an exothermic process. Furthermore, this phenomenon is very dependent on the shape of the sample and boundary conditions [30, 31]: it is why the fronts generally propagate from the jaws, due to tightening. This topic is currently trendy and more and more simulations are able to predict this phenomenon [32–35].

These three phenomena are generally not considered simultaneously to numerically predict the vibratory response of cables equipped with SMA-based dampers [36–38]. The main target of the paper is to propose such a numerical tool while accurately predicting a realistic behavior of the embedded NiTi wires. In the "Experiments and modeling" section, the experimental set-up and the corresponding numerical modeling are briefly presented. In the "Results and discussion" section, several numerical configurations are compared with the experimental results, to determine the contribution of each considered phenomenon. Eventually, data available numerically only are investigated to provide a better understanding.

2. Experiments and modeling

In this section, the proposed experimental set-up and Finite Element model are presented in parallel. Firstly, the vibrating cable is considered alone. Secondly, installation of the damping device on the cable is presented. Thirdly, the thermomechanical behavior of the embedded NiTi components is dealt with. Eventually, the post-processing procedure is detailed to show how will be conducted the analysis in the "Results and discussion" section.

2.1. Full-scale bridge cable

2.1.1. Experimental set-up

A cable of length $L = 50$ m was used to measure the efficiency of the NiTi-based damping device. An axial tensile force T of approximatively 900 kN was initially applied to the cable using a hydraulic jack. It must be noted that the study cases that are proposed in this paper are intentionally simplified in comparison with the loading cases experienced by cable structures in service. First, to involve the minimum number of vibration modes, punctual deviations were applied on the cable at $L/2$ or $L/4$, by applying a transverse force of 4 kN. Secondly, the force was suddenly released using an electromagnet to make the cable freely vibrating. The vibration problem is assumed to be in-plane. The cable composition and properties are given in [10].

Since $EI << TL^2$, where EI is the flexural rigidity of the cable, a good approximation of the $n-th$ mode frequency is given by [39]:

$$f_n = \frac{n}{2L}\sqrt{\frac{T}{\mu}}\left[1 + 2\sqrt{\frac{EI}{TL^2}} + \left(4 + \frac{n\pi^2}{2}\right)\frac{EI}{TL^2}\right] \approx \frac{n}{2L}\sqrt{\frac{T}{\mu}} \tag{2.1}$$

With μ the linear density of the cable. The values of the analytical modal frequencies can be used as a validation criteria of modeling. Cable transverse displacements were measured with laser sensors at three locations along the cable ($L/2$, $L/4$ and $L/16$).

2.1.2. Numerical modeling

Modeling of the cable was performed using the Finite Element Method with the MSC Marc industrial code [40]. In the proposed model, only beam or truss elements were considered, since dynamic simulations require substantial computing resources. The cable consisted of 50 two-node Euler-Bernoulli beam elements. Both nodes located at the extremities of the cable were clamped (fixed degrees of freedom). An initial pre-stress corresponding to the 900 kN pretension was applied to the beam elements. The simulation was split into two parts: (i) a transverse force was progressively and slowly applied on a node until 4 kN (quasi-static formulation), (ii) the force was suddenly released (dynamic formulation) and the cable was freely vibrating for 20 s. The intrinsic damping ratio ξ of the cable due to internal frictions was estimated from experimental transverse displacement signals of the cable without any damping device using the logarithmic decrement method. A Rayleigh viscous damping was assigned on the whole cable elements to provide intrinsic damping capacity. The Rayleigh damping matrix is given by:

$$[C] = \alpha\,[M] + \beta\,[K] \tag{2.2}$$

Where $[M]$ and $[K]$ are the mass and stiffness matrices involved in the motion equilibrium equation, respectively. The coefficients $\alpha = 7.52\ 10^{-3} s^{-1}$ and $\beta = 1.43\ 10^{-5} s$ were calculated from the ξ value of 0.00033 [40].

2.1.3. Validation of the cable vibrating response

Figure 1a,c,d present the numerical and experimental transverse displacement of the cable at $L/2$, $L/4$ and $L/16$, respectively, while the transverse force was placed at $L/2$. Figure 1b provides the Fast

Fourier Transform (FFT) spectra associated with the signals presented in Figure 1a.

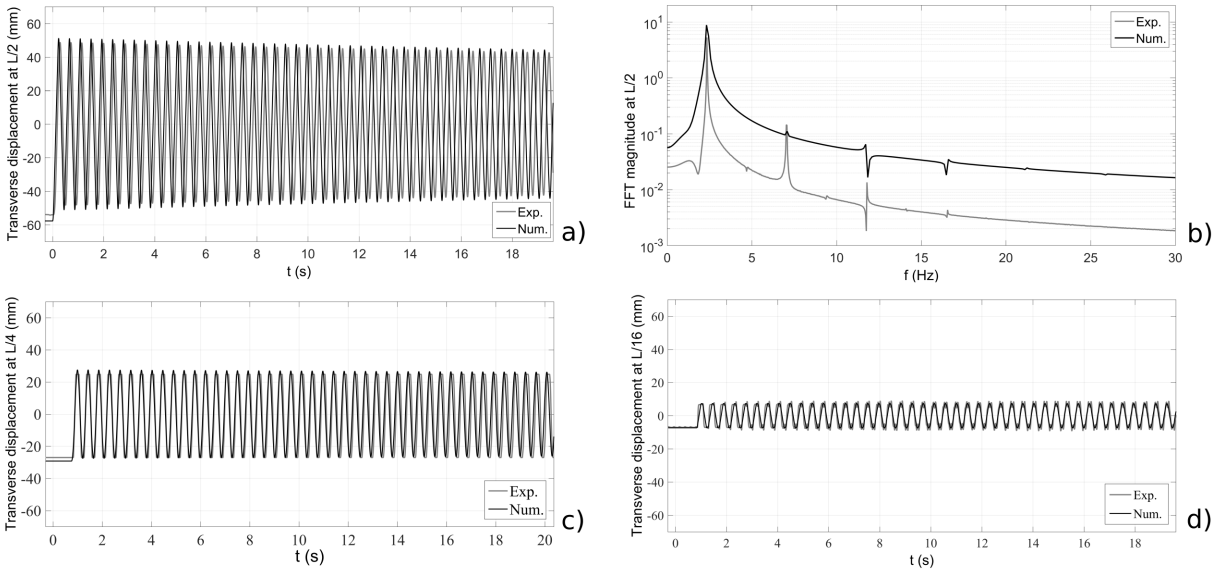

Figure 1. Transverse displacement of the cable (transverse force at $L/2$): (a) at L/2; (b) associated FFT frequency spectra; (c) at L/4; (d) at L/16.

The signals numerically obtained are in good agreement with the experimental signals, whatever the considered location. The frequency spectrum numerically obtained shows a good prediction of the contributions of the vibration modes. The first mode associated with a frequency value of about 2.3 Hz (as verified using Eq 2.1) had the highest contribution, since the force was placed at the corresponding anti-node. It slightly overestimated the experimental values. From the simulations, only odd-numbered modes were observable, since $L/2$ is the common node for even-numbered modes.

2.2. Design and installation of the damper

2.2.1. Developed damping device

Figure 2a presents the developed damping device. Two plates are crossed by NiTi wires. One plate was clamped to the ground, while the second plate was linked with the cable. The wires were elongated thanks to mechanical stops placed at the exterior side of each plate. Thus, the damper worked in one direction only (when the cable was moving away from the anchorage), but this system prevented wires from buckling. Figure 2b presents its installation on the full-scale cable.

The chemical composition (56.30 wt% Ni) of the NiTi alloy used in this work is detailed in [15]. The characteristic temperature A_f was measured at about 5 °C. NiTi wires were "trained" under cyclic mechanical loadings at room temperature (100 tensile cycles of 8% strain amplitude at a frequency of 0.0056 Hz) before being embedded in the damping device to limit residual strain [10]. Two wires of diameter 2.46 mm and effective length 1260 mm were embedded to reach a maximal relative elongation of 2% in service. Furthermore, the NiTi wires were pre-strained thanks to a turnbuckle system (see Figure 2a). An initial elongation of about 4 mm was chosen to increase the dissipation (for a given room temperature and a given deviating force value) as explained in [41].

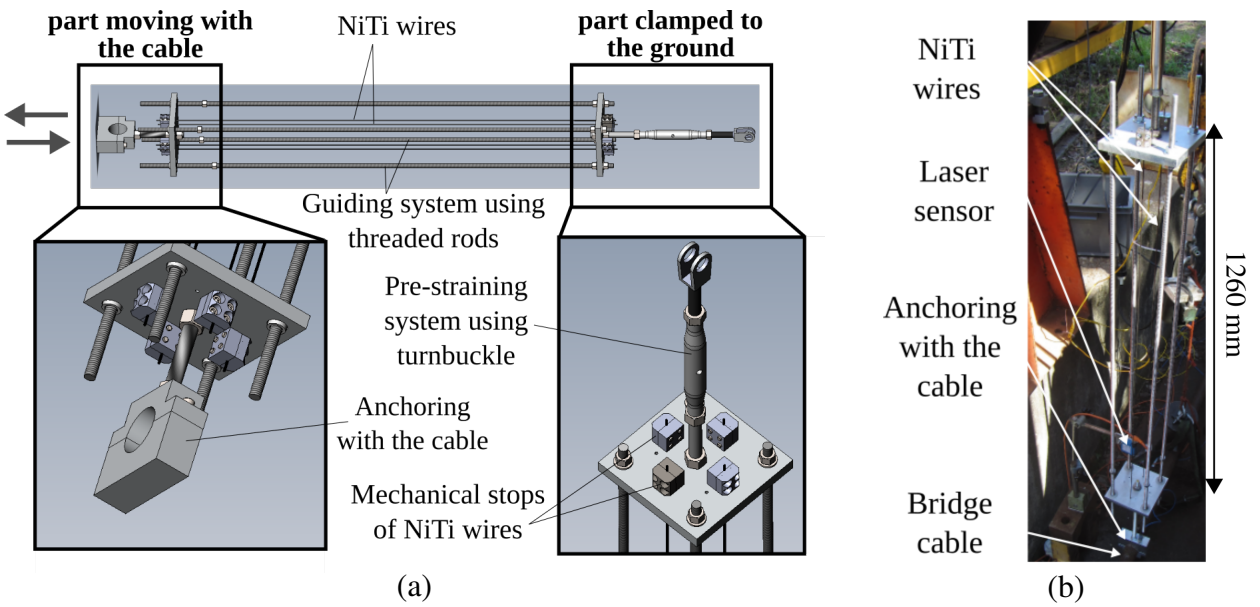

Figure 2. Damping device: (a) Scheme of the device, (b) installation on the full-scale cable.

For the sake of simplicity, the damping device was placed far from the anchorages to better understand the influence of the damper on the whole cable response. Three study cases were investigated to change the contribution of the involved vibration modes:

(1) Damper & force at $L/2$ (reference).

(2) Damper at $L/4$ and force at $L/2$.

(3) Damper at $L/2$ and force at $L/4$.

The study case of reference is investigated in detail in this study.

2.2.2. Numerical assembly of the damper on the cable

Figure 3 describes the modeling of the "cable-damper" system. The damping device consisted of one or 32 (as explained later) two-node thermomechanical truss elements assembled in series. The length of the "numerical damper" was the same as the effective length of the two NiTi wires embedded in the damping device. Its cross-section area was taken as the sum of the cross-section areas of the two wires, since they work in tension. The node at one end of the wire was fixed to the ground, while the node at the opposite end was connected with one of the nodes of the cable thanks to a spring of infinite stiffness working in the transverse direction of the cable. The selected node of the cable depends on the damper position. The stiffness of the damper was canceled in case of negative stress values to deactivate it under compression loadings. The pre-strain of the numerical damper was imposed during the very first calculation step.

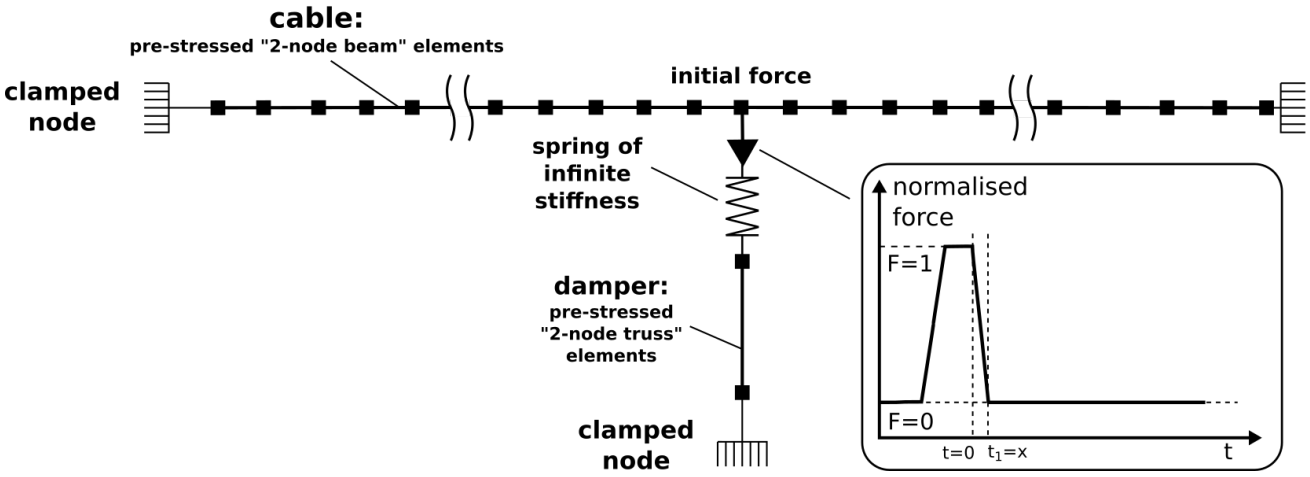

Figure 3. Scheme of the Finite Element model of the whole system "damper+cable".

2.3. NiTi wire behavior law

2.3.1. Material behavior law

The behavior law used in what follows was presented in detail in [42]. Since the "numerical damper" was modeled by truss elements, the behavior law was written in a uniaxial version. Its role is to compute the uniaxial stress σ and tangent modulus values from the current strain ε and strain increment $\Delta\varepsilon$ values. The internal variables are $z^M \in [0;1]$ and $z^R \in [0;1]$ which are the martensite and R-phase volume fractions, respectively. The austenite volume fraction is therefore given by $z^A = 1 - z^M - z^R$.

The proposed model was based on four yield surfaces, associated with yield functions $f_1^M(M)$ and $f_2^M(M,X)$, driving the forward and reverse austenite-to-martensite transformations, respectively, and $f_3^R(R)$ and $f_4^R(R,Y)$, driving the forward and reverse austenite-to-R-phase transformations, respectively. M and X are isotropic and kinematic "pseudo-hardening" functions of z^M associated with the austenite-to-martensite transformation, respectively. R and Y are isotropic and kinematic "pseudo-hardening" functions of z^R associated with austenite-to-R-phase transformation, respectively. The transformation yield stresses σ_0^M and σ_0^R were linear functions of the material temperature T.

The heat equation was derived from the formulated specific free energy by applying the principle of energy conservation. It involves the exchanges with the exterior by diffusion and convection, as well as the dissipation and thermomechanical coupling terms associated with both transformations.

For details on the identification procedure of the material parameters and on the model validation, the reader is referred to [42]. For this present work, the thermo-mechanical behavior law was implemented in a user subroutine coded in FORTRAN [40]. The retained material parameters corresponding to a trained NiTi wire are set out in Table 1 [43].

Table 1. Material parameters corresponding to a trained NiTi alloy.

E_A	E_M	γ_M	ω^{min}	ω^{max}	M^{max}	σ_0^M	μ^M	λ
57.0	21.6	4.9	150	20	20	340	6.3	18.0
(GPa)	(GPa)	(%)	(MPa)	(MPa)	(MPa)	(MPa)	(MPa · K^{-1})	(W · m^{-1}· K^{-1})

ρ	E_R	γ_R	δ^{min}	δ^{max}	R^{max}	σ_0^R	μ^R	C_p
6450	40.4	0.25	15	15	220	156	13.45	500
(kg · m^{-3})	(GPa)	(%)	(MPa)	(MPa)	(MPa)	(MPa)	(MPa · K^{-1})	(J · K $^{-1}$· kg^{-1})

2.3.2. Strain localization along the NiTi wire

As the wire model was reduced to one dimension to restrict the computational time, the strain localization effect (associated with 3D effects) along the wire had to be considered by other means. To take into account the propagation of martensitic transformation bands, a non-local model was implemented using the Finite Element method [43]. 32 thermomechanical two-node truss elements were used and assembled as presented in Figure 4. The analysis presented in the "Results and discussion" section focuses on three reference positions associated with elements 2, 4 and 12.

Figure 4. Three reference positions along the numerical wire.

Instead of using the nominal stress σ in the material behavior law, an apparent stress value σ_{app} was computed for each element. It enabled us to take into account the effect of the high shear stress values at the interface between phases, in addition to the tensile stress value. Thus, it was assumed that the propagation was driven by the maximal stress value at the interface between a wire portion of martensite and a wire portion of austenite. The apparent stress of a given element m was calculated using a stress intensity factor $K_I(m)$:

$$\sigma_{app}(m) = \sigma K_I(m) \tag{2.3}$$

By assuming a linear bi-material perfectly bonded cylinder to represent the stress intensity at the interface between these two portions, the value of K_I should be a function of the stiffness properties on both sides of the interface [44]. To facilitate the convergence of the model and to consider the specific case of the element m ($1 < m < 32$), a function K_I^* of z_m^M, z_{m-1}^M and z_{m+1}^M the martensite volume fraction of the element m and its neighbors $m-1$ and $m+1$, respectively, was introduced:

$$K_I^*(m) = 1 + max\left(\left\langle z_{m+1}^M - z_m^M \right\rangle, \left\langle z_{m-1}^M - z_m^M \right\rangle\right)\left(K_I^0 - 1\right) \tag{2.4}$$

Where $\langle x \rangle$ is equal to x if $x \geq 0$ and is equal to 0 if $x < 0$. Thus, $K_I^*(m) = 1$ if the m element is in the same state as its direct neighbors, and $K_I^*(m) = K_I^0$ if the m element is in the austenitic state and one of its neighbors is fully martensitic. The constant value of $K_I^0 = 1.6$ was chosen, in agreement with the results presented in [29]. Since bands propagation has never been observed in the case of R-phase transformation, the R-phase volume fraction was not considered in Eq 2.4.

In order to study the effect of the clamping of the jaws on the stress at the ends of the wire, it can be assumed that the wire corresponds locally to a solid cylinder subjected to an external pressure. Thus, the calculation of radial and orthoradial stresses from Lamé's equations allows to show that clamping under a pressure of P_0 induces a reduction of the equivalent Von Mises stress by a stress corresponding to P_0 [45]. The consequence is that the tightening effect in the jaws can be simulated in a uniaxial model by increasing the initial axial stress value of the elements placed at the two ends of the wire. To respect forces equilibrium and to avoid any technical issues, it was prefered to decrease the transformation yield stresses in these two elements (n° 1 and 32). The values of $\sigma_0^{M,R} - 100MPa$ was retained to ensure an initial state without martensite.

The model was validated by a force-imposed tensile test to the maximal value of 2600 N, over a cycle with a frequency of 3 Hz, which is an order of magnitude equivalent to the first modal frequency of the cable. The results are presented in Figure 5a,b. Figure 5a confronts the numerical stress-strain curve to the experimental one by considering strain localization or not. Figure 5b presents the local mechanical behavior observed numerically in several elements along the wire, for the configuration where strain localization was considered.

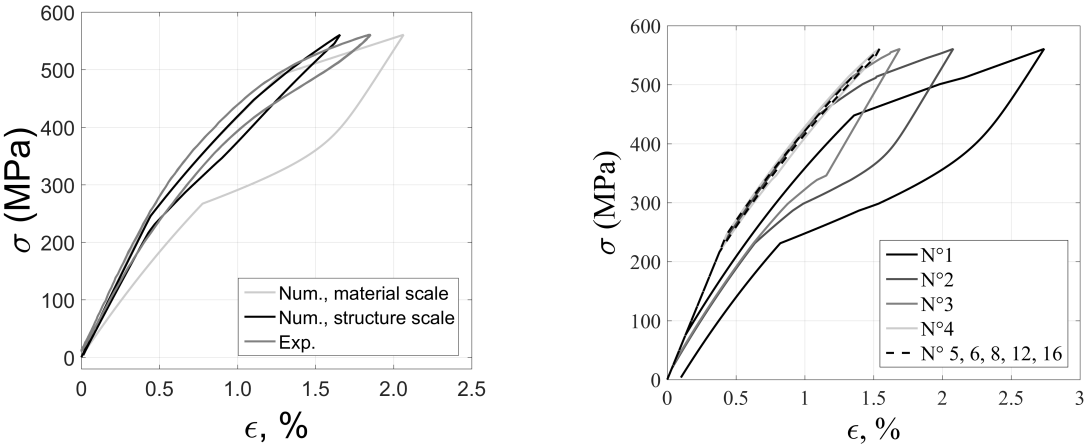

(a) (b)

Figure 5. (a) Stress-strain curve for a force-imposed test by considering bands propagation (wire scale) or no propagation (material scale); (b) corresponding behavior of several elements along the wire structure.

From Figure 5a, the prediction of mechanical behavior was improved by considering strain localization. Due to the propagation of the martensitic transformation bands from the anchorages, the closer the elements to the anchorages, the more they experienced martensitic transformation (see Figure 5b). However, all the elements experienced R-phase transformation. In particular, elements 5 to 16 (and their symmetrical elements 17 to 28) underwent only this intermediate transformation, which resulted in thin hysteresis loops.

2.3.3. Numerically studied configurations

Table 2 presents the five studied configurations confronted in this paper. These configurations represent different levels of complexity: configuration 1 is associated with an elastic behavior of the damper

(material in a pure austenitic state), while configuration 5 is associated with a superelastic behavior taking all the identified phenomena into account. All the retained configurations are presented successively to discuss the contribution of each added phenomenon.

Table 2. Studied material configurations.

Configuration	Superelasticity	R-phase	Thermal effects	Strain localization	Number of elements for the damper
1	n	n	n	n	1
2	y	n	n	n	1
3	y	y	n	n	1
4	y	y	y	n	1
5	y	y	y	y	32

2.4. Post-processing

To carefully analyze the influence of the material behavior of the NiTi wires embedded in the damper on the dynamic response of the whole cable structure, it was necessary to select relevant indicators related to both scales.

First, the dynamic response of the cable was investigated. Equation 2.5 is the general form of the cable transverse displacement law $y(x,t)$, which assumes heterogeneous properties along the cable due to a punctual influence of the damping device [41].

$$y(x,t) = \sum_{n=1}^{N} C_n(x,t)\, \sin\left(\frac{n\pi x}{L}\right) \sin\left(2\pi f_n(x,t)\sqrt{1-\xi_n^2(x,t)}t + \phi_n(x,t)\right) \exp\left(-2\pi f_n(x,t)\xi_n(x,t)t\right) \quad (2.5)$$

With f_n the natural frequency, ξ_n the damping ratio, C_n the modal contribution in the time domain, ϕ_n the phase related to each mode n. The following modal parameters (identified from Eq 2.5) were computed over time, as in [41]:

- $f_1(x,t)$, the natural frequency related to the first vibration mode by applying a Wigner-Ville transform on the transverse displacement signal at $x = L/2$, using a Matlab toolbox provided by [46],
- $\xi_1(x,t)$, the damping ratio related to the first vibration mode by plotting $ln(env(y_1))$ the logarithm of the signal envelop after numerical filtering to isolate the first mode: the damping ratio changes correspond to the slope changes on the computed curve.

The beginning of the curves presented later were affected by side effects due to numerical filtering.

Secondly, an investigation based on the material behavior performed numerically was carried. Thus, the changes in material temperature T and volume fraction of the phases (z^M and z^R) were plotted. The loss factor was computed from strain-stress numerical values over time to quantify the damping capacity of the material. It is linked to the material dissipated energy (through ΔW corresponding to the hysteresis loop area on the stress-strain curve) and the strain energy (through W corresponding to the area below the transformation path on the same curve), after Eq 2.6 [47].

$$\eta = \frac{1}{2\pi}\frac{\Delta W}{W - \frac{1}{2}\Delta W} \quad (2.6)$$

One can say that the loss factor does not directly correspond to the damping ratio computed from the cable displacement signal, even if both are naturally linked. However, it is a precious indicator to identify the different potential damping regimes.

3. Results and discussion

In this section, the five considered configurations are presented in the reference study case. For each configuration, the transverse displacement of the cable at $L/2$ (damper and deviating force position) numerically obtained was compared to the experimental signal for 20 s from the moment the force is released. The corresponding material behavior is presented for three arbitrarily chosen time windows: (i) [0–1] s, (ii) [2–3.5] s, (iii) [19–20] s. The window of [2–3.5] s corresponded approximatively to the transition between the two first damping regimes, whatever the configuration. Since temperature has a great influence on NiTi behavior, it is important to specify that all the tests were performed at a testing temperature of about 20 °C (±2 °C).

The signals were centered on the "zero" value, which means that the cable remained at a displacement value of zero before any deviating force application. In the particular case where the wires would have not been pre-strained, the positive values of the transverse displacement measured at the damper position would have corresponded to activation stages of the device. On the contrary, negative values would have been associated with deactivation stages. By pre-straining the wires, the transition associated with the deactivation of the device is expected to be shifted to the negative values. For an initial elongation of 4 mm, this transition should be close to the value of −4 mm.

To focus the analysis on the influence of the behavior of the NiTi wires on the damping capacity of the device, the study case of reference is presented in this section and the attention is paid on the cable displacement at the force and damper position. Additional results associated with the dynamic response along the cable for the different study cases are presented in the Appendixes.

3.1. Influence of thermal effects and R-phase transformation (configurations 2, 3, 4/study case 1)

3.1.1. Results

Figures 6, 7a, 8a and 9a provide the transverse displacement of the cable at $L/2$, for configurations 1, 2, 3 and 4, respectively. The material behavior associated with the "numerical damper" is given in Figures 7b–d, 8b–d, and 9b–d, for configurations 2, 3 and 4, respectively.

From Figure 6, the experimental signal illustrates a high and quite regular decrease in displacement amplitude. The cable almost reached equilibrium after 20 s following the release of the force.

By considering an elastic behavior of the numerical damper (configuration 1), no energy was dissipated. Thus, the damping capacity provided by the numerical damper was almost zero, accordingly (see Figure 6). The small damping observable was due to the intrinsic damping of the cable. However, the additional stiffness of the elastic damper enabled to "cut" the signal parts associated with the activation stages of the damper, while the signal parts associated with the deactivation stages were not affected. Eventually, the displacement amplitude was decreased compared to the configuration without any damping device (see Figure 1a) but the dynamic response obtained numerically did not reproduce the experimental signal.

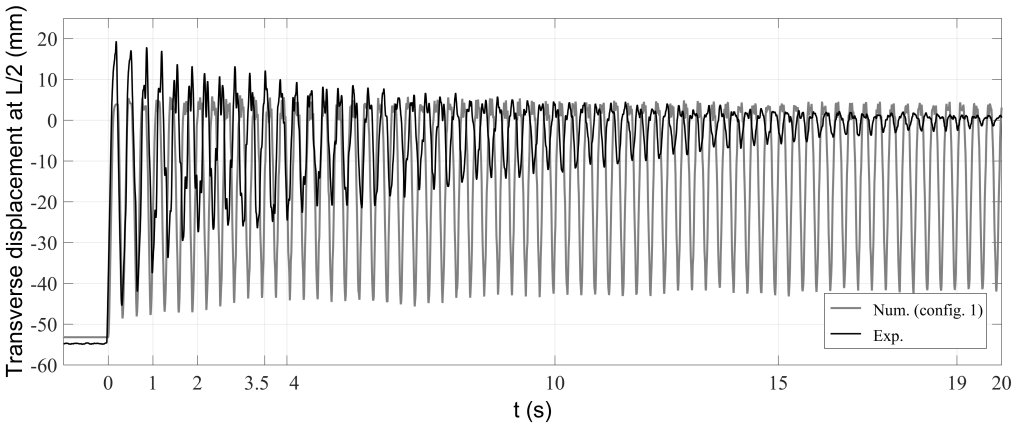

Figure 6. Transverse displacement of the cable at L/2 equipped with a damper (study case 1/configuration 1) placed at L/2.

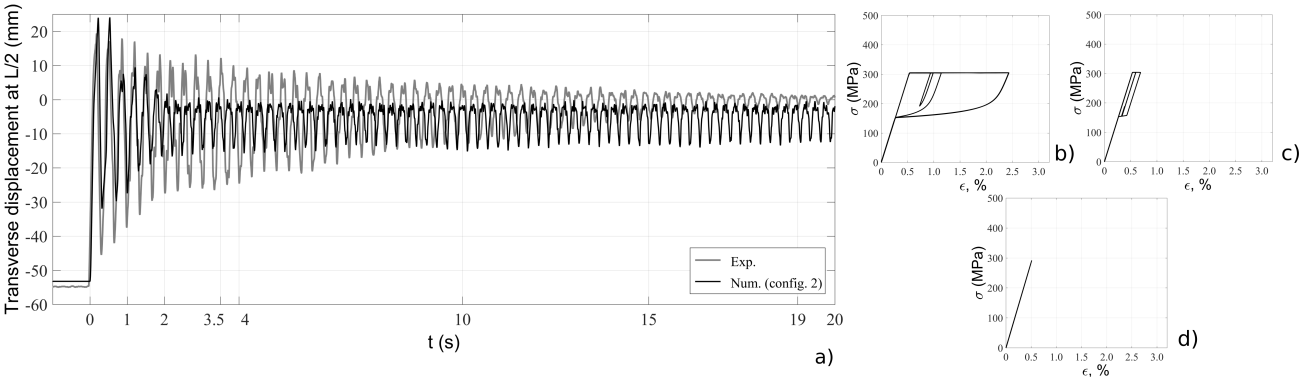

Figure 7. (a) Transverse displacement of the cable at L/2 equipped with a damper (study case 1/ configuration 2) placed at L/2; Stress-Strain curves related to the behavior of the material embedded in the damper: (b) [0, 1]s, (c) [2, 3.5]s , (d) [19, 20]s.

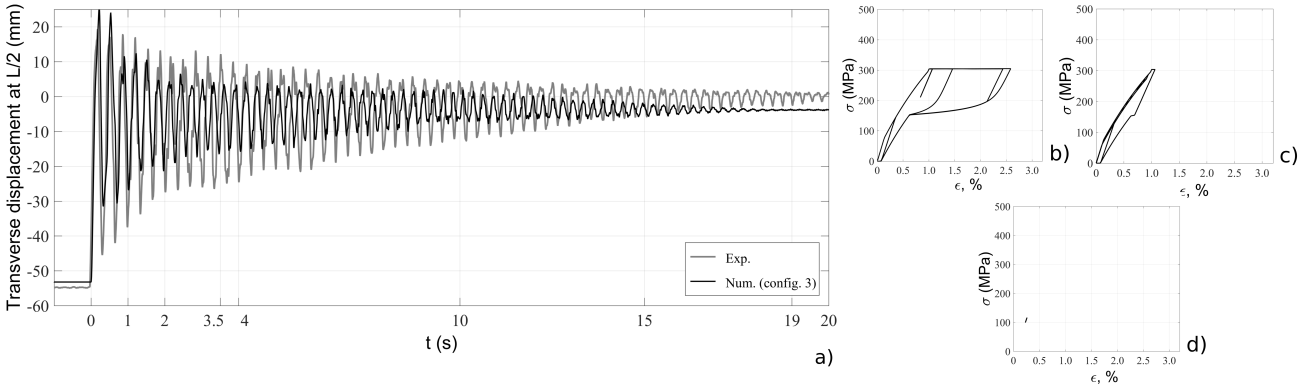

Figure 8. (a) Transverse displacement of the cable at L/2 equipped with a damper (study case 1/configuration 3) placed at L/2; Stress-Strain curves related to the behavior of the material embedded in the damper: (b) [0, 1]s, (c) [2, 3.5]s , (d) [19, 20]s.

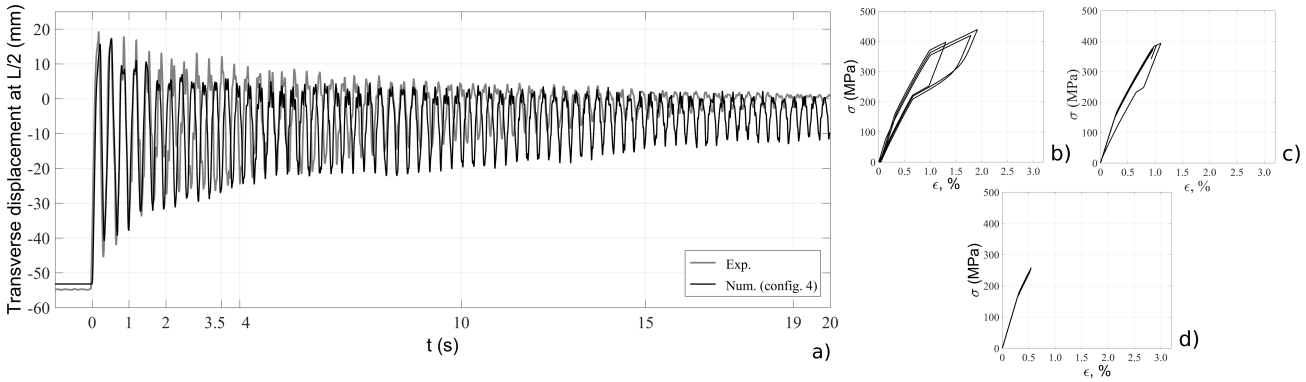

Figure 9. (a) Transverse displacement of the cable at L/2 equipped with a damper (study case 1/ configuration 4) placed at L/2; Stress-Strain curves related to the behavior of the material embedded in the damper: (b) [0, 1]s, (c) [2, 3.5]s , (d) [19, 20]s.

By considering the superelasticity effect (configuration 2), a strong mitigation of the cable amplitude was observed within the first 3 s following the force release (see Figure 7a). After this first damping stage, the displacement amplitude remained constant ("undamped stage"). These observations are in agreement with the corresponding behavior of the wire. The first stage was associated with transformation into martensite (see Figure 7b,c). Once the amplitude was associated with a maximal stress value inferior to the martensite transformation yield stress value, the amplitude remained almost constant (see Figure 7d). Eventually, the response prediction was greatly improved compared to configuration 1. However, the damping capacity was overestimated during the first part of the signal and underestimated during the following part.

By considering the intermediate R-phase transformation (configuration 3), the first damping stage observed in the previous configuration was affected and an intermediate damping stage appeared, as highlighted in Figure 8a. During the first stage, austenite transformed into R-phase before martensite appearance over the loading cycles: for a given level of wire elongation, the dissipated energy decreased when compared to a material without R-phase transformation (see Figure 8b,c). In the second stage, once the loading amplitude corresponded to a maximal stress value inferior to the martensitic transformation yield stress value, the R-phase transformation still operated alone. It explains why a second and low damped stage appeared. Furthermore, the yield stress value associated with the transformation into R-phase is low at room temperature (inferior to 100 MPa). Thus, stabilization of the cable was achieved after 20 s following the force release. One can observe that the final material state obtained numerically corresponded to an elastic behavior associated with a mixture of austenite and R-phase, due to the NiTi wires pre-strain (see Figure 8d). Due to this pre-strain, the final undamped stage was not observed unlike in configuration 2: the fully austenite elastic state could not be reached. Eventually, damping capacity was overestimated during the whole signal, although it has decreased during the first damping stage compared to configuration 2.

By considering the thermal effects (configuration 4), the first and second damping stages observed previously still operated but their respective damping capacity decreased compared to configuration 3 (see Figure 9a). From Figure 9b,c, the combination of thermomechanical couplings and intrinsic dissipation involved an increase in both martensitic plateau slope and martensitic transformation yield stress. Considering the present material, a decrease in damping performance under these loading con-

ditions (frequency and amplitude) is in agreement with results reported in [15]. The combination of both transformation into R-phase and thermal effects provided a much better prediction of the first damping stage (see Figure 9a) compared to the previous configurations. However, the second damping stage was underestimated, despite R-phase transformation.

3.1.2. Discussion

Figure 10a–c provides z^M, z^R and T changes over time, while Figure 11a–c compares f_1, $ln(env(y_1)$ (from the cable scale) and η (from the material scale) for configurations 2 to 4. For reasons of readability, only the first 10 s are plotted, in what follows.

From Figure 10a, no martensite appeared after $t = 4$ s, whatever the configuration. From Figure 10a,b, less martensite appeared when R-phase was taken into account (as reflected by a lower maximal martensite volume fraction in configurations 3 and 4). By considering R-phase transformation, the latter was observed at least during the first 10 s after the force release, in both configurations 3 and 4. These comments directly explain why a lower damping ratio during the first damping stage and a higher damping ratio during the next one were observed in configuration 3 compared to configuration 2. In configuration 4, phase transformations naturally entailed material temperature changes (see Figure 10c): in the first stage, quite high thermal variations associated with the latent heat of the martensitic transformation and a self-heating due to intrinsic dissipation were observed in parallel. The temperature logically inhibited the transformation of austenite into R-phase and martensite by increasing the associated transformation yield stresses (see Figure 10a). In the second stage, lower thermal variations (mainly due to the thermomechanical couplings associated with transformation into R-phase only) were highlighted. However, the intrinsic dissipation associated with the intermediate transformation did no longer override thermal exchanges with the surroundings: a return to the thermal equilibrium was therefore observed. This decrease in temperature favored occasional martensite formation and maintained the amount of R-phase approximatively constant, as observed in Figure 10a,b.

From Figure 11a, a large gap can be measured between the frequency values obtained numerically by configuration 2 on one hand, and configurations 3 and 4 on the other hand. This is probably due to a difference in additional stiffness brought to the cable, associated with transformation into R-phase in the NiTi wires. Indeed, the latter was not considered in configuration 2. Another large gap can be measured between the frequency values obtained numerically in configurations 3 and 4 and the experimental values. That could be due to the fact that the stiffness associated with the mechanical parts clamped to the ground and to the moving cable (see device in Figure 2a) were not considered in the modeling. Indeed, these parts are deformable and not infinitely stiff. This should not entail significant consequences on the damping prediction because the strain rates experienced by the NiTi wires remained of the same order of magnitude. This is why the attention should be only paid on the relative increases in frequency values. The frequency changes were best reproduced by configuration 4, where a smooth increase in f_1 was observed. It can be explained by a better prediction of the behavior of the embedded material compared to configurations 2 and 3, and consequently by a better prediction of the stiffness added to the cable.

From Figure 11b,c, a first damping stage can be clearly identified from 0 to about 3–4 s in configurations 2 and 3, from the point of view of both the vibrating structure ($ln(env(y_1))$) and the material behavior (η). It directly corresponds to the transformation into martensite. Without taking R-phase into account, the first damping stage was followed by an undamped stage, where the material behavior be-

came elastic (configuration 2). A better prediction of the damping capacity was observed in the second damping stage thanks to R-phase transformation, that occurred at least 10 s after the force release and induced a low but non zero energy dissipation (configuration 3). From Figure 11b,c, damping capacity was more distributed over time in configuration 4, by taking into account thermal effects that smoothed the damping ratio changes. Eventually, a better prediction of the damping capacity is also observed in configuration 4.

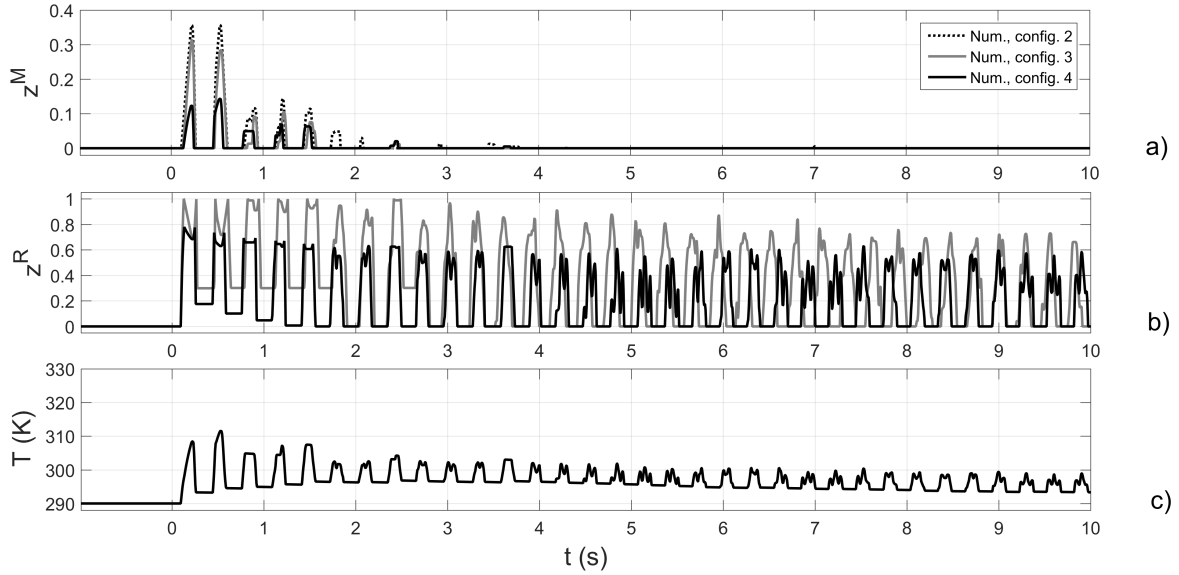

Figure 10. Comparison between configurations 2, 3, 4: (a) martensite volumic fraction; (b) R-phase volumic fraction; (c) material temperature.

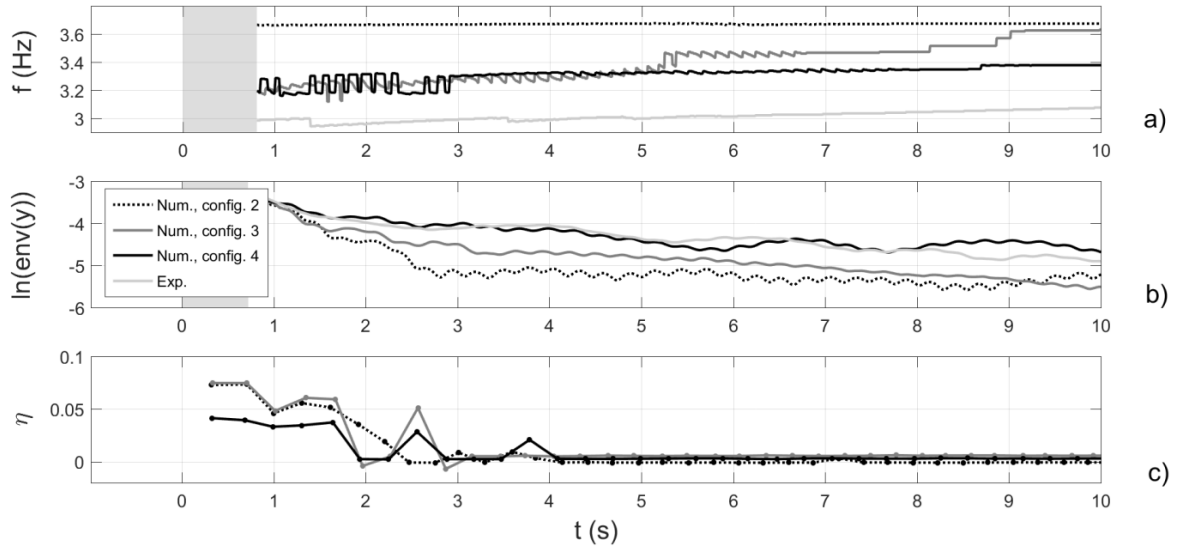

Figure 11. Comparison between configurations 2, 3, 4: (a) frequency of the 1^{st} mode; (b) logarithm of the signal envelop; (c) loss factor η.

Up to this point, configuration 4 provided the best prediction, while the computing time was reasonable since the numerical damper consisted of one truss element only. The next and last configuration should improve the prediction but should also require more computational resources, by splitting the numerical damper into 32 truss elements to take the strain localization phenomenon into account. Thus, configuration 4 should be seriously considered for further works, regardless of the results associated with configuration 5.

3.2. Influence of strain localization (configuration 4, 5/study case 1)

3.2.1. Results

Figure 12a provides the transverse displacement of the cable at $L/2$ for configuration 5, while the material behavior associated with the "numerical damper" is presented for three elements along the wire (see Figure 4) in Figure 12b–d. The macroscopic behavior resulting from the contribution of all the elements along the wire is given in Figure 12e.

Configuration 5 provided by far the best agreement with the transverse displacement signal obtained experimentally (see Figure 12a), despite a small gap at the end of the signal due to a possible accumulation of residual strain in the wires (blocked martensite) as the experiments progressed. The obtained macroscopic behavior of the wire was much smoother than material behaviors observed in the previous configurations, due to the average of the local behaviors. Furthermore, the transitions between the different damping regimes are difficult to identify, as in the experimental signal. From Figure 12b,c, the dissipated energy was locally high at the extremities of the wire compared to the average dissipated energy (see Figure 12e) or to the dissipated energy obtained from the single "damper" element in configuration 4 (see Figure 9b). It is quite easy to explain: the transformation bands propagated from the extremities of the wires. This point is very important and highlights an advantage of configuration 5 over configuration 4: taking into account heterogeneities in the thermomechanical behavior along the wire enables to better predict the maximal stress and dissipated energy values experienced by the wires to therefore estimate the fatigue life of the damping device. It would be a great assistance to optimize the design of the damper. Eventually, the last configuration improved the vibrating response of the whole system.

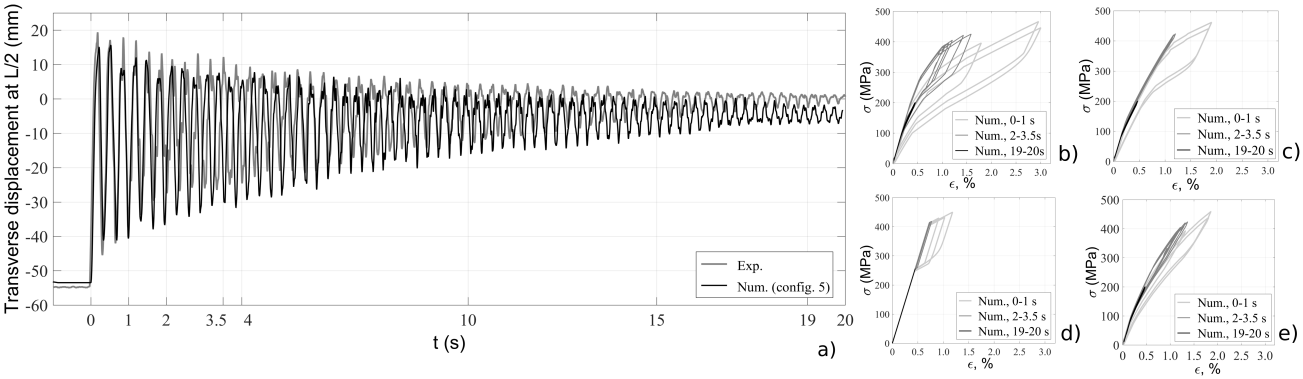

Figure 12. (a) Transverse displacement of the cable at L/2 equipped with a damper (study case 1/configuration 5) placed at L/2; Stress-Strain curves related to the local behavior of the material embedded in the damper at three reference positions: (b) element n° 2, (c) n° 4, (d) n° 12, (e) macroscopic behavior of the wire.

3.2.2. Discussion

Figure 13a–c provides z^M, z^R and T changes over time, while Figure 14a–c compares f_1, $ln(env(y_1)$ (from the structure point of view) and η (from the material point of view), for configurations 4 and 5. In configuration 5, only values associated with the same elements as those described previously are presented. One can add that η was computed from the macroscopic behavior of the whole wire in configuration 5.

From Figure 13a, the elements that are close to the anchorages experienced more martensite transformation (and therefore dissipated more energy), since propagation of transformations bands was restricted to a very limited wire portion: due to high strain rate values, a high increase in temperature near the transformation fronts inhibited transformation into martensite beyond the front. It is confirmed by higher maximal martensite volume fraction and temperature values in element 2 for configuration 5, than in the single element for configuration 4.

This strain localization explains the decrease in damping capacity provided by configuration 5 compared to configuration 4, as observed in Figure 14a–c. Indeed, the material heterogeneity induced a distribution of the damping capacity over time. In particular, the transitions between the distinct damping regimes in configuration 4 are no longer observable in configuration 5, according to the changes in damping ratio and loss factor highlighted in Figure 14b,c. However, no significant improvement of the stiffness and damping ratio in the prediction over time was provided by configuration 5. Eventually, the main difference between configurations 4 and 5 lies in the prediction of the local behavior of the material in order to study its damage and fatigue life.

In order to fully validate the numerical tool, it was necessary to study the response of the cable at positions different from that of the damper. The two others study cases and additional results regarding the reference study case are briefly presented in Appendixes. Both configurations 4 and 5 showed good agreements with the experimental curves.

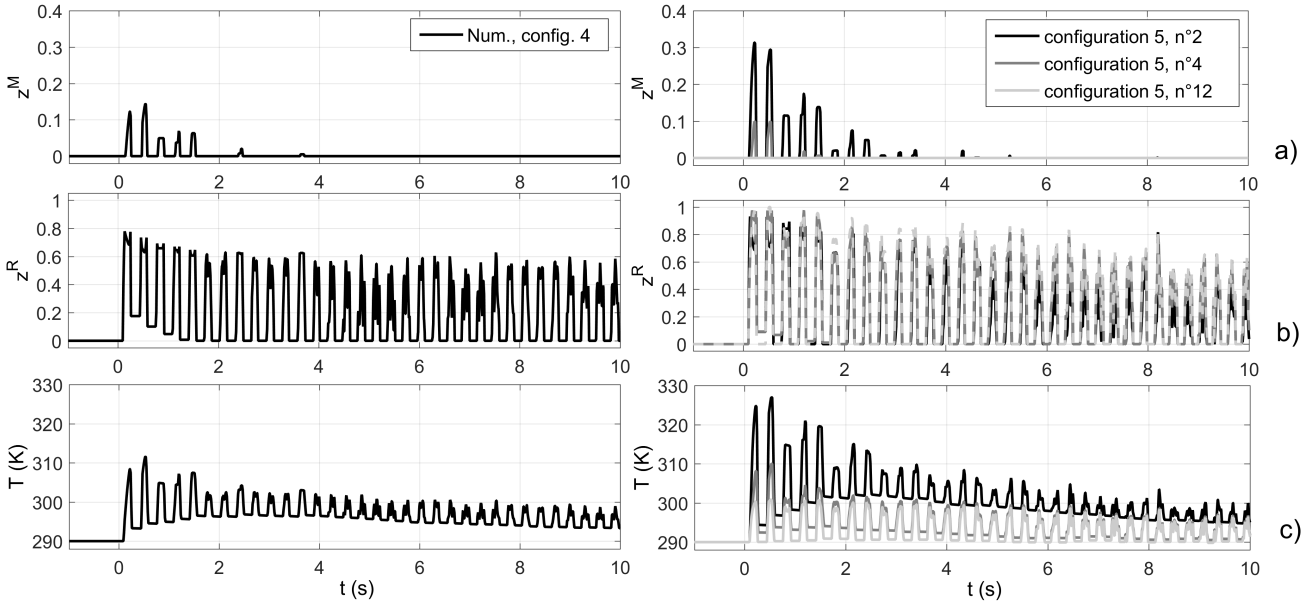

Figure 13. Comparison between configurations 4 and 5: (a) martensite volumic fraction; (b) R-phase volumic fraction; (c) material temperature.

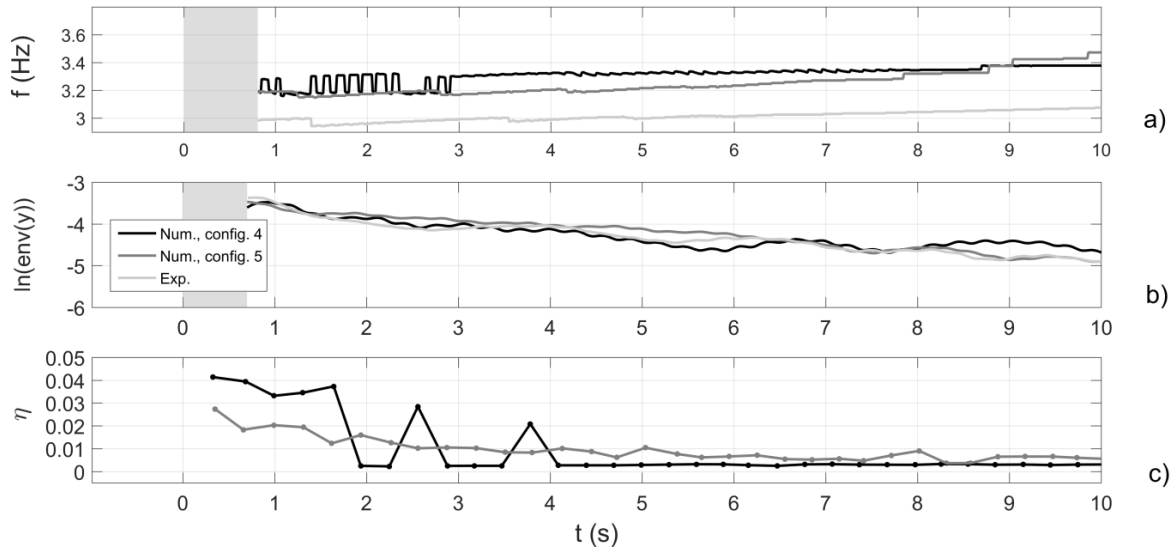

Figure 14. Comparison between configurations 4 and 5: (a) frequency of the 1^{st} mode; (b) logarithm of the signal envelop; (c) loss factor η.

4. Conclusions

In conclusion, the following points can be highlighted:

- A numerical tool was developed to predict the dynamic response of a cable equipped with a NiTi wire-based damping device and was validated using three study cases (where the contribution of the different modes was different).
- In particular, the influence of the material behavior of the NiTi wires embedded in the damping device was investigated. To do this, several configurations taking into account the phenomena that influence the energy dissipated by these wires were studied. The importance of taking both the thermal effects, the intermediate R-phase transformation and the strain localization into account was demonstrated.
- Two configurations (4 and 5) that proved to be the best to predict damping capacity of the damper were studied in detail. Their respective interest was discussed. For instance, configuration 4 (thermal effects and intermediate R-phase transformation) requires less computing resources and can be used to optimize the damping setting-up (by acting on the effective length and number/section of the wires, pre-strain of the wires, position of the damping device along the cable), since these optimization procedures are computationally intensive. Configuration 5 that takes propagation of transformation bands into account in addition to the previous phenomena provided a better description of the material behavior along the wire by discretizing it into several elements. It can roughly be used for optimization, but the fatigue life of the embedded wires can be considered to dimension the device regarding its service life, in addition to its effectiveness.

Several perspectives have been identified to pursue this work:

- More realistic loading cases experienced by cables should be studied, such as harmonic or random forced loadings, punctual or distributed heterogeneously along the cable.

- The numerical tool should be used to define the tuning of the damping device setting-up according to the constraints of a given structure (angle of the cable chord, natural frequency of the cable, kind of solicitations).
- The link between the dissipated energy by NiTi alloys and their fatigue resistance should be investigated to be considered in the optimization of NiTi-based damping devices.
- Heterogeneity of the material behavior (due to propagation of transformation bands) should be investigated to optimize damping capacity and fatigue resistance. For instance, periodic localized cross-section decrease and/or stress increase, modification of clamping system or well-suited thermomechanical training could be considered.

Acknowledgments

To Daniel Bruhat, Richard Michel, Jean-François David and Yannick Falaise (MAST/Université Gustave Eiffel) for their participation in the experimental set-up, the development of the damping device and the measurements.

Conflict of interest

The authors declare that they have no known competing financial interests or personal relationships that could have appeared to influence the work reported in this paper.

References

1. Ungar EE, Kerwin EM (1962) Loss factors of viscoelastic systems in terms of energy concepts. *J Acoust Soc Am* 34: 954–957. https://doi.org/10.1121/1.1918227
2. Cai J, Mao S, Liu Y, et al. (2022) Nb/NiTi laminate composite with high pseudoelastic energy dissipation capacity. *Mater Today Nano* 19: 100238. https://doi.org/10.1016/j.mtnano.2022.100238
3. Oliveira JP, Zeng Z, Berveiller S, et al. (2018) Laser welding of Cu–Al–Be shape memory alloys: Microstructure and mechanical properties. *Mater Design* 148: 145–152. https://doi.org/10.1016/j.matdes.2018.03.066
4. Patoor E, Berveiller M (1994) *Les Alliages à Mémoire de Formes*, Hermes.
5. Otsuka K, Wayman C (1998) *Shape Memory Materials*, Cambridge: Cambridge University Press.
6. Udovenko VA (2003) Damping, In: Brailovski V, Prokoschkin S, Terriault P, et al., *Shape Memory Alloys Fundamentals, Modelling and Applications*, University of Quebec, Montreal, Canada, 279–309.
7. Orgéas L, Favier D (1998) Stress-induced martensitic transformation of a NiTi alloy in isothermal shear, tension and compression. *Acta Mater* 46: 5579–5591.
8. Menna C, Auricchio F, Asprone D (2014) Application of shape memory alloys in structural engineering, In: Lecce L, Concilio A, *Shape Memory Alloy Engineering: for Aerospace, Structural and Biomedical Applications*, Elsevier, 369–403. https://doi.org/10.1016/B978-0-08-099920-3.00013-9

9. Matsumoto M, Daito Y, Kanamura T, et al. (1998) Wind-induced vibration of cables of cable-stayed bridges. *J Wind Eng Ind Aerod* 74: 1015–1027. https://doi.org/10.1016/S0167-6105(98)00093-2
10. Dieng L, Helbert G, Arbab Chirani S, et al. (2013) Use of shape memory alloys damper device to mitigate vibration amplitudes of bridge cables. *Eng Struct* 56: 1547–1556. https://doi.org/10.1016/j.engstruct.2013.07.018
11. Nespoli A, Rigamonti D, Riva M, et al. (2016) Study of pseudoelastic systems for the design of complex passive dampers: static analysis and modeling. *Smart Mater Struct* 25: 105001. https://doi.org/10.1088/0964-1726/25/10/105001
12. Tobushi H, Shimeno Y, Hachisuka T, et al. (1998) Influence of strain rate on superelastic properties of TiNi shape memory alloys. *Mech Mater* 30: 141–150. https://doi.org/10.1016/S0167-6636(98)00041-6
13. Liu Y, Favier D (2000) Stabilisation of martensite due to shear deformation via variant reorientation in polycrystalline NiTi. *Acta Mater* 48: 3489–3499. https://doi.org/10.1016/S1359-6454(00)00129-4
14. Bouvet C, Calloch S, Lexcellent C (2004) A phenomenological model for pseudoelasticity of shape memory alloys under multiaxial proportional and nonproportional loadings. *Eur J Mech A-Solid* 23: 37–61. https://doi.org/10.1016/j.euromechsol.2003.09.005
15. Helbert G, Saint-Sulpice L, Arbab Chirani S, et al. (2014) Experimental characterisation of three-phase NiTi wires under tension. *Mech Mater* 79: 85–101. https://doi.org/10.1016/j.mechmat.2014.07.020
16. Zhu S, Zhang Y (2007) A thermomechanical constitutive model for superelastic SMA wire with strain-rate dependence. *Smart Mater Struct* 16: 1696. https://doi.org/10.1088/0964-1726/16/5/023
17. Heintze O, Seelecke S (2008) A coupled thermomechanical model for shape memory alloys-From single crystal to polycrystal. *Mater Sci Eng A-Struct* 481–482: 389–394. https://doi.org/10.1016/j.msea.2007.08.028
18. Shariat BS, Liu Y, Rio G (2012) Thermomechanical modelling of microstructurally graded shape memory alloys. *J Alloys Compd* 541: 407–414. https://doi.org/10.1016/j.jallcom.2012.06.027
19. Xiao Y, Zeng P, Lei L (2019) Micromechanical modelling on thermomechanical coupling of superelastic NiTi alloy. *Int J Mech Sci* 153–154: 36–47. https://doi.org/10.1016/j.ijmecsci.2019.01.030
20. Otsuka K, Ren X (2005) Physical metallurgy of Ti-Ni-based shape memory alloys. *Prog Mater Sci* 50: 511–678. https://doi.org/10.1016/j.pmatsci.2004.10.001
21. Oliveira JP, Mirande RM, Braz Fernandez FM (2017) Welding and joining of NiTi shape memory alloys: A review. *Prog Mater Sci* 88: 412–466. https://doi.org/10.1016/j.pmatsci.2017.04.008
22. Šittner P, SedlákP, Landa M, et al. (2006) In situ experimental evidence on R-phase related deformation processes in activated NiTi wires. *Mater Sci Eng A-Struct* 438–440: 579–584. https://doi.org/10.1016/j.msea.2006.02.200
23. Sengupta A, Papadopoulos P (2009) Constitutive modeling and finite element approximation of B2-R-B19' phase transformations in Nitinol polycrystals. *Comput Method Appl M* 198: 3214–3227. https://doi.org/10.1016/j.cma.2009.06.004

24. Sedlák P, Frost M, Benešová B, et al. (2012) Thermomechanical model for NiTi-based shape memory alloys including R-phase and material anisotropy under multi-axial loadings. *Int J Plast* 39: 132–151. https://doi.org/10.1016/j.ijplas.2012.06.008

25. Rigamonti D, Nespoli A, Villa E, et al. (2017) Implementation of a constitutive model for different annealed superelastic SMA wires with rhombohedral phase. *Mech Mater* 112: 88–100. https://doi.org/10.1016/j.mechmat.2017.06.001

26. Zhou T, Yu C, Kang G, et al. (2020) A crystal plasticity based constitutive model accounting for R phase and two-step phase transition of polycrystalline NiTi shape memory alloys. *Int J Solids Struct* 193–194: 503–526. https://doi.org/10.1016/j.ijsolstr.2020.03.001

27. Shaw JA, Kyriakides S (1995) Thermomechanical aspects of NiTi. *J Mech Phys Solids* 43: 1243–1281. https://doi.org/10.1016/0022-5096(95)00024-D

28. Favier D, Louche H, Schlosser P, et al. (2007) Homogeneous and heterogeneous deformation mechanisms in an austenitic polycrystalline Ti-50.8 at% Ni thin tube under tension. Investigation via temperature and strain fields measurements. *Acta Mater* 55: 5310–5322. https://doi.org/10.1016/j.actamat.2007.05.027

29. Sedmák P, Pilch J, Heller L, et al. (2016) Grain-resolved analysis of localized deformation in nickel-titanium wire under tensile load. *Science* 353: 559–562. https://doi.org/10.1126/science.aad6700

30. He YJ, Sun QP (2010) Rate-dependent domain spacing in a stretched NiTi strip. *Int J Solids Struct* 47: 2775–2783. https://doi.org/10.1016/j.ijsolstr.2010.06.006

31. Shariat BS, Bakhtiari S, Yang H, et al. (2020) Controlled initiation and propagation of stress-induced martensitic transformation in functionally graded NiTi. *J Alloys Compd* 851: 156103. https://doi.org/10.1016/j.jallcom.2020.156103

32. Sun QP, Zhong Z (2000) An inclusion theory for the propagation of martensite band in NiTi shape memory alloy wires under tension. *Int J Plast* 16: 1169–1187. https://doi.org/10.1016/S0749-6419(00)00006-1

33. Chan CW, Chan SHJ, Man HC, et al. (2012) 1-D constitutive model for evolution of stress-induced R-phase and localized Lüders-like stress-induced martensitic transformation of super-elastic NiTi wires. *Int J Plast* 32–33: 85–105. https://doi.org/10.1016/j.ijplas.2011.12.003

34. Soul H, Yawny A (2013) Thermomechanical model for evaluation of the superelastic response of NiTi shape memory alloys under dynamic conditions. *Smart Mater Struct* 22: 035017. https://doi.org/10.1088/0964-1726/22/3/035017

35. Xiao Y, Jiang D (2020) Constitutive modelling of transformation pattern in superelastic NiTi shape memory alloy under cyclic loading. *Int J Mech Sci* 182: 105743. https://doi.org/10.1016/j.ijmecsci.2020.105743

36. Zuo XB, Li AQ (2011) Numerical and experimental investigation on cable vibration mitigation using shape memory alloy damper. *Struct Control Health Monit* 18: 20–39.

37. Ben Mekki O, Auricchio F (2011) Performance evaluation of shape-memory-alloy superelastic behavior to control a stay cable in cable-stayed bridges. *Int J Non-Linear Mech* 46: 470–477. https://doi.org/10.1016/j.ijnonlinmec.2010.12.002

38. Torra V, Auguet C, Isalgue A, et al. (2013) Built in dampers for stayed cables in bridges via SMA. The SMARTeR-ESF project: A mesoscopic and macroscopic experimental analysis with numerical simulations. *Eng Struct* 49: 43–57. https://doi.org/10.1016/j.engstruct.2012.11.011

39. Morse P, Ingard K (1968) *Theoritical Acoustics*, Princeton University Press.

40. MSC (2008) *Marc/mentat volume A: Theory and user information*.

41. Helbert G, Dieng L, Arbab Chirani S, et al. (2018) Investigation of NiTi based damper effects in bridge cables vibration response: Damping capacity and stiffness changes. *Eng Struct* 165: 184–197. https://doi.org/10.1016/j.engstruct.2018.02.087

42. Helbert G, Saint-Sulpice L, Arbab Chirani S, et al. (2017) A uniaxial constitutive model for superelastic NiTi SMA including R-phase and martensite transformations and thermal effects. *Smart Mater Struct* 26: 025007. https://doi.org/10.1088/1361-665X/aa5141

43. Helbert G (2014) *Contribution à la durabilité des câbles de Génie Civil vis-à-vis de la fatigue par un dispositif amortisseur à base de fils NiTi*, Université de Bretagne Sud.

44. Qian ZQ, Akisanya AR (1999) An investigation of the stress singularity near the free edge of scarf joints. *Eur J Mech A-Solid* 18: 443–463. https://doi.org/10.1016/S0997-7538(99)00118-7

45. Harvey JF (1974) *Theory and Design of Modern Pressure Vessels*, Van Nostrand Reinhold.

46. Auger F, Gonçalvès P, Lemoine O, et al. (1996) Time-frequency toolbox: For use with Matlab. Available from: https://tftb.nongnu.org/

47. Piedboeuf MC, Gauvin R, Thomas M (1998) Damping behaviour of shape memory alloys: strain amplitude, frequency and temperature effects. *J Sound Vib* 214: 895–901. https://doi.org/10.1006/jsvi.1998.1578

Appendix

A. Damper at L/2 and deviation at L/2 (study case 1)

Figure 15a,b provides cable transverse displacements at $L/4$ and $L/16$, while the force and the damper were placed at $L/2$.

For both positions $L/4$ and $L/16$, a good agreement is observed between numerical and experimental results. In [41], the authors distinguished the local effect of the damper (due to a punctual increase of the stiffness near the device) from the global effect (function of the distance from the antinodes of the considered modes). These results validate how the cable and the damper were connected in the Finite Element model.

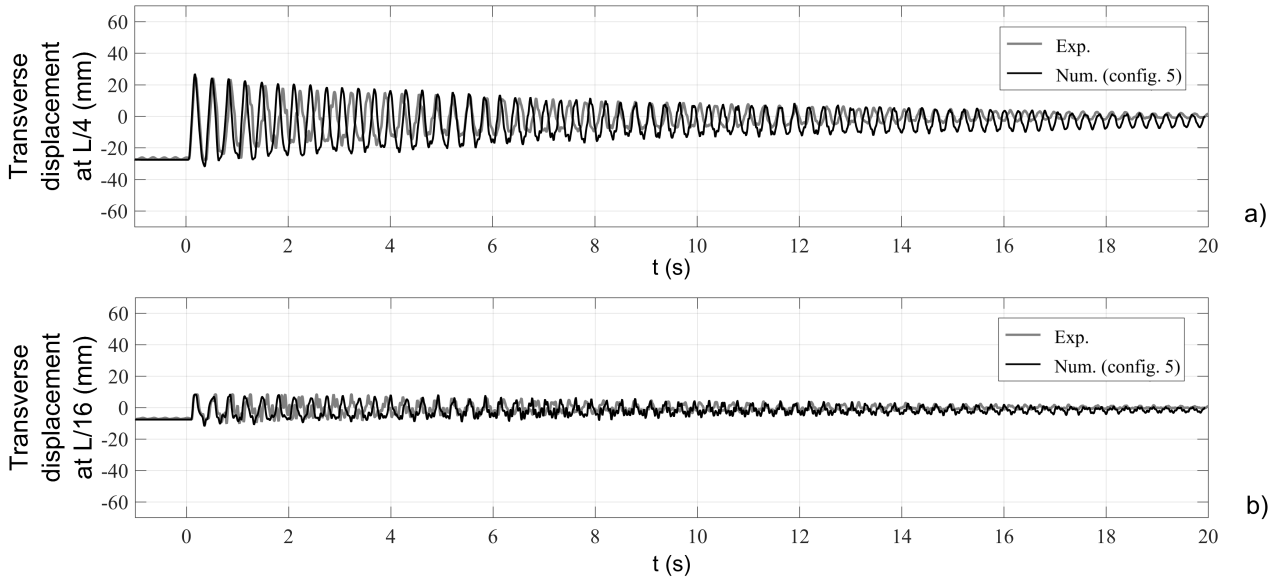

Figure 15. Transverse displacement of the cable equipped with a damper (configuration 5) placed at L/2: (a) sensor at L/4, (b) sensor at L/16.

B. Damper at L/4 and deviation at L/2 (study case 2)

Figure 16a–c provides the cable transverse displacement at $L/2$, $L/4$ and $L/16$, while the damper was moved to $L/4$.

It should be noted that the sensor placed at $L/2$ was an accelerometer for this study case. The transverse displacement signal obtained experimentally was integrated from the transverse acceleration and information was lost during numerical integrations. It explains why the initial deviation before the cable release is not observable (see Figure 16a). This point is not a major problem since the initial deviation is similar to those obtained in study case 1 (the deviating force was placed at the same position and the initial deviation was associated with the deactivated stage of the damper). A very good agreement is observed between numerical and experimental results in both configurations, although configuration 4 overestimated the damping even more than configuration 5. One can observe a lower damping compared to the reference study case. Indeed, the damping device was no longer placed at the antinode of the first and main involved vibration mode in study case 2.

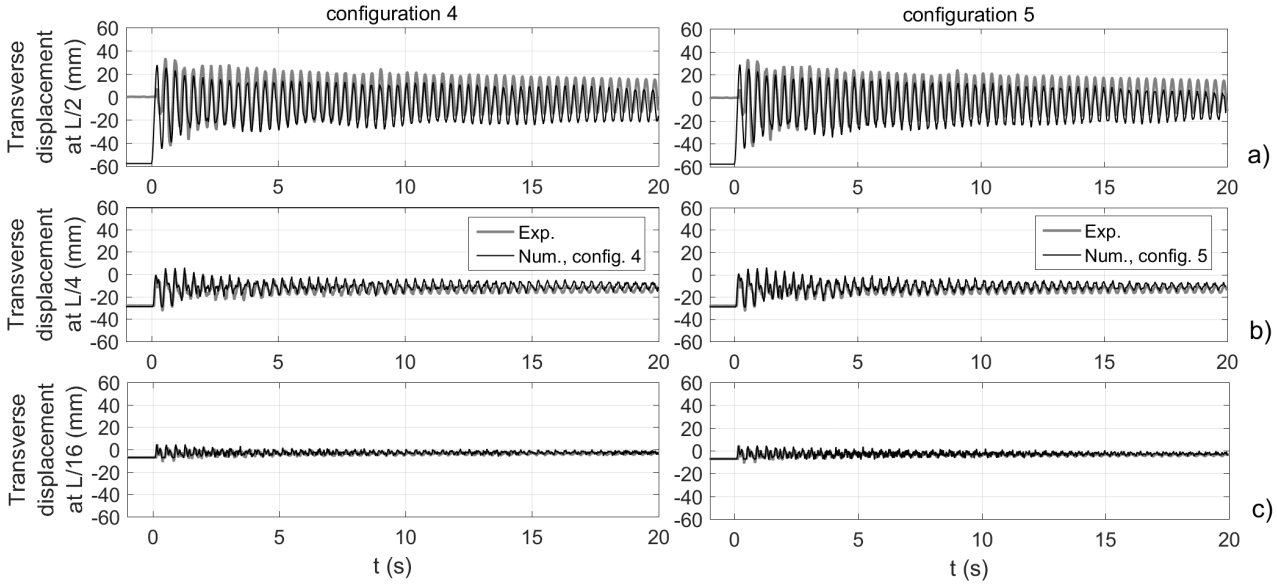

Figure 16. Transverse displacement of the cable equipped with a damper placed at L/4: sensor placed (a) at L/2, (b) at L/4, (c) at L/16.

C. Damper at L/2 and deviation at L/4 (study case 3)

Figure 17a–c provides the cable transverse displacement at $L/2$, $L/4$ and $L/16$, while the force was moved to $L/4$ and the damper was placed at $L/2$. This study case is the least favorable with respect to the second vibration mode since the force was placed at its antinode and the damper was placed at its node.

From Figure 17a–c, a strong damping was observed experimentally and numerically at $L/2$ where was placed the damper, while a low damping was observed at $L/4$ and $L/16$ where the second vibration mode had a higher contribution. This confirms that placing the device in the middle of the cable is not relevant regarding the even-numbered modes. For both configurations 4 and 5, a good agreement is observed regarding the transverse displacement amplitude and its mitigation. However, an offset can be observed regarding the initial amplitude at $L/2$ and $L/4$, whatever the configuration. This offset can be explained by a small error on the pre-strain value of the "numerical wire" due to the potential accumulation of residual strain in the wires during the test campaign or a small error on the cable bending stiffness. Once again, a better damping prediction was obtained in configuration 5.

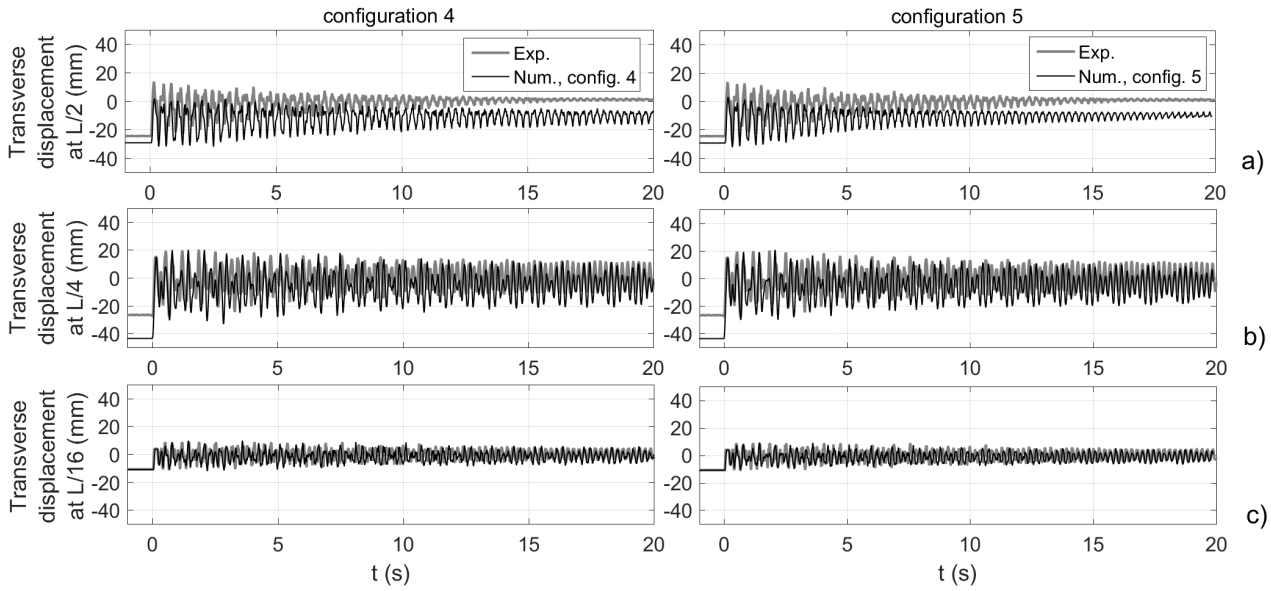

Figure 17. Transverse displacement of the cable equipped with a damper placed at L/2: sensor placed (a) at L/2, (b) at L/4, (c) at L/16.